

## Reflection imaging of aseismic zones of the Nazca slab by global-phase seismic interferometry

Nishitsuji, Yohei; Ruigrok, E; Gomez, M; Wapenaar, Kees; Draganov, Deyan

**DOI**

[10.1190/INT-2015-0225.1](https://doi.org/10.1190/INT-2015-0225.1)

**Publication date**

2016

**Document Version**

Accepted author manuscript

**Published in**

Interpretation

**Citation (APA)**

Nishitsuji, Y., Ruigrok, E., Gomez, M., Wapenaar, K., & Draganov, D. (2016). Reflection imaging of aseismic zones of the Nazca slab by global-phase seismic interferometry. *Interpretation*, 4(3), SJ1-SJ16. <https://doi.org/10.1190/INT-2015-0225.1>

**Important note**

To cite this publication, please use the final published version (if applicable). Please check the document version above.

**Copyright**

Other than for strictly personal use, it is not permitted to download, forward or distribute the text or part of it, without the consent of the author(s) and/or copyright holder(s), unless the work is under an open content license such as Creative Commons.

**Takedown policy**

Please contact us and provide details if you believe this document breaches copyrights. We will remove access to the work immediately and investigate your claim.

**Full title: Reflection Imaging of Aseismic Zones of the Nazca slab by Global-phase  
Seismic Interferometry**

Author's names: Yohei Nishitsuji<sup>1\*</sup>, Elmer Ruigrok<sup>2</sup>, Martín Gomez<sup>3</sup>, Kees Wapenaar<sup>1</sup>,  
Deyan Draganov<sup>1</sup>

Affiliation: <sup>1</sup>Department of Geoscience and Engineering,

Delft University of Technology, Delft, The Netherlands

<sup>2</sup>Department of Earth Sciences,

Utrecht University, Utrecht, The Netherlands;

R&D Seismology and Acoustics, Royal Netherlands Meteorological  
Institute (KNMI), De Bilt, The Netherlands

<sup>3</sup>International Center for Earth Sciences,

Comision Nacional de Energia Atomica, Buenos Aires, Argentina

Date of submission: 30-Dec, 2015

Abbreviated title: Reflection imaging of aseismic zones

Corresponding author:

name : Yohei Nishitsuji

address: Department of Geoscience and Engineering,

Delft University of Technology

Stevinweg 1, 2628 CN Delft, Netherlands

P.O. Box 5048, 2600 GA Delft, Netherlands

email : [y.nishitsuji@tudelft.nl](mailto:y.nishitsuji@tudelft.nl)

## 1 **Abstract**

2 Obtaining detailed images of aseismic parts of subducting slabs remains a large  
3 challenge for understanding slab dynamics. Hypocenter mapping cannot be used for  
4 the purpose due to the absence of seismicity, while the use of receiver functions might  
5 be compromised by the presence of melt. Global tomography can be used to identify  
6 the presence of the slab, but does not reveal its structure in detail. Here, we show how  
7 detailed images can be obtained using global-phase seismic interferometry. The  
8 method provides high-resolution ( $< 15$  km in depth) pseudo zero-offset (i.e., co-located  
9 source and receiver) reflection information. We apply the method to aseismic zones of  
10 the Nazca slab where initiation of possible slab tearing and plume decapitation are  
11 identified by global tomography and electrical conductivity, respectively. We obtain an  
12 image of the Moho and the mantle, and find an attenuated area in the image consistent  
13 with the presence of an aseismic dipping subducting slab. However, the interpretation is  
14 not unambiguous. The results confirm that the method is useful for imaging aseismic  
15 transects of slabs.

16

## 17 INTRODUCTION

18           It has been shown that at the northern part of Central Chile (30 - 33°S) the  
19 Nazca slab is of the flat type (e.g., Rosenbaum et al., 2005; Anderson et al., 2007;  
20 Eakin et al., 2014). At that part, the upwelling plume was recently imaged (Booker et  
21 al., 2004). Still, the slab's geometry in the southern part of central Chile (34 - 37°S) is  
22 unclear and it is unknown whether that part of the slab is not torn (e.g., Gilbert et al.,  
23 2006; Pesicek et al., 2012).

24           One of the challenges in imaging the slab in this region by seismological  
25 methods relates to the absence of seismicity. Although hypocenter mapping is a useful  
26 method for identifying the Wadati-Benioff zone (e.g., Cahill and Isacks, 1992;  
27 Syracuse and Abers, 2009; Bloch et al., 2014), it cannot be used to image the aseismic  
28 region.

29           The receiver-function method (e.g., Langston 1979; Audet et al., 2009;  
30 Kawakatsu and Yoshioka, 2011) can be used to image aseismic regions, but so far has  
31 not yielded images of the aseismic zone in this region. Yuan et al. (2000) suggest that  
32 the reason for this might be the possible completion of the gabbro-eclogite

33 transformation within the Nazca slab. Gilbert et al. (2006) suggest large attenuation of  
34 *S*-wave energy in the mantle wedge as another possible reason.

35 Global tomography (e.g., Aki et al., 1977; Dziewonski et al., 1977; Boschi  
36 and Becker, 2011) is a tool for investigating global-scale geodynamics and it can be  
37 used for imaging aseismic zones. However, the method's resolution ( $\approx 50$  km) poses  
38 limitations on estimating the slab's exact location and continuity at local scale, thus  
39 leaves a lot of uncertainties.

40 The reflection method with active sources (explosives, vibroseis, airguns)  
41 provides the needed high-resolution imaging capabilities, but its depth penetration is  
42 fundamentally limited by the strength of the used sources.

43 Here, we demonstrate the usefulness of an alternative seismic technique to  
44 image the aseismic slab zone with high resolution, namely seismic interferometry (SI)  
45 for body-wave retrieval (e.g., Claerbout, 1968; Scherbaum, 1987a,b; Daneshvar et al.,  
46 1995; Wapenaar, 2003) using global phases (GloPSI) (Ruigrok and Wapenaar, 2012).  
47 Global phases are seismic phases that travel through the Earth's core before reaching  
48 the surface. They are induced by earthquakes at epicentral distances greater than  $120^\circ$

49 (global distances). The global phases are extracted from the continuous field  
50 recordings and used as contributions from separate transient sources. For the  
51 considered configuration, this is closely related to work of Kumar and Bostock (2006)  
52 and Nowack et al. (2007). For a horizontally layered (1D) acoustic medium, SI  
53 retrieves the reflection response of the medium from the autocorrelation of the  
54 medium's plane-wave transmission response measured at the surface (Claerbout,  
55 1968). GloPSI is a 3D generalization of the mentioned 1D case – it extends the  
56 illumination to include a range of ray parameters (horizontal slownesses) allowing  
57 retrieval of reflections from 3D structures. At seismic stations, these extra ray  
58 parameters would come from recorded global P-wave arrivals, such as the phases *PKP*,  
59 *PKiKP*, and *PKIKP*. These arrivals (phases) have ray parameters lower than 0.04 s/km  
60 and are characterized in the mantle by nearly planar wavefronts. This makes these  
61 phases suitable for SI by autocorrelation. Due to the autocorrelation, GloPSI retrieves  
62 pseudo zero-offset reflection arrivals that penetrate deep enough to allow slab imaging  
63 with resolution dictated by the frequency bandwidth of the phases, sensor  
64 configuration and two-way travelttime difference between consecutive arrivals. GloPSI

65 may further shed light on one of the open questions in the geoscience community of  
66 whether small deformations and/or detachments ( $< 25$  km) in the slab are actually  
67 present (Wortel and Spakman, 2000).

68 In the following, we show how to apply GloPSI to field waveform data. First  
69 we describe the GloPSI method, then we describe the data we use, phase extraction and  
70 preparation, and then we show our results and their interpretation. Our results image  
71 the aseismic zone of the slab and possible deformation in the slab.

72

## 73 **Global-phase seismic interferometry (GloPSI)**

### 74 **Theory**

75 The 1D theory from Claerbout (1968) was generalized for a 3D  
76 inhomogeneous medium by Wapenaar (2003). Ruigrok and Wapenaar (2012) applied  
77 the generalization of seismic interferometry for retrieval of body waves from the  
78 autocorrelation of global phases recorded at seismic stations in Himalaya and Tibet.  
79 They termed this specific application GloPSI.

80 The GloPSI relation for the retrieval of the zero-offset reflection response

81  $R(\mathbf{x}_R, \mathbf{x}_R, t)$  for co-located source and receiver at the location of station  $\mathbf{x}_R$  is

82 (Ruigrok and Wapenaar, 2012)

83

$$84 \sum_{p_{\min}}^{p_{\max}} \sum_{\theta_{\min}}^{\theta_{\max}} \left\{ T(\mathbf{x}_R, \mathbf{p}_S, -t) * T(\mathbf{x}_R, \mathbf{p}_S, t) * E_i(-t) * E_i(t) \right\} \propto \left\{ \delta(t) - R(\mathbf{x}_R, \mathbf{x}_R, -t) - R(\mathbf{x}_R, \mathbf{x}_R, t) \right\} * \bar{E}_n(t), \quad (1)$$

85

86 where  $T(\mathbf{x}_R, \mathbf{p}_S, t)$  is the transmission response (selected global phase) at the receiver

87 location  $\mathbf{x}_R$  due to an earthquake  $i$ , arriving from direction  $\mathbf{p}_s = (p, \theta)$  with ray

88 parameter  $p$  and back azimuth  $\theta$ ,  $E_i(t)$  is the source time function of the  $i$ -th

89 earthquake,  $\bar{E}_n(t)$  is the average of the autocorrelations of the different source time

90 functions, and  $*$  denotes convolution. In our case, the absolute value of the ray

91 parameter varies between 0 and 0.04 s/km, while  $\theta$  varies between  $0^\circ$  and  $360^\circ$ . In

92 equation (1), the summation is effectively over plane-wave sources, instead of over

93 point sources. A derivation of the SI relation from point sources to plane-wave sources

94 can be found in Ruigrok et al. (2010). The zero-offset reflection response retrieved by

95 GloPSI can be used to image the subsurface structures in a way similar to the

96 conventional reflection seismic method with active sources. Note that GloPSI directly

197 produces zero-offset reflection responses of the subsurface, which is one of the  
198 conventional goals of the active-source reflection method. With the latter, offset  
199 measurements are stacked to obtain pseudo zero-offset traces (Yilmaz, 1987), as direct  
100 zero-offset measurements are still commercially impractical. A difference between the  
101 zero-offset section retrieved by GloPSI and an active-source pseudo zero-offset section  
102 is that the virtual source in the former radiates energy vertically and near-vertically  
103 down into the Earth, while in the latter the pseudo zero-offset source radiates in all  
104 directions. Because of this, GloPSI will image horizontal to mildly inclined structures  
105 directly, while steeply dipping structures will be manifest by a lack of reflections  
106 reaching the receivers and can be interpreted by discontinuation of imaged (nearly)  
107 horizontal structures. This is similar to the problem in the active-source reflection  
108 method, where a steeply dipping structure lying relatively deep compared to the  
109 receiver-array length, will not be imaged (e.g., Yilmaz, 1987).

110           When the length of the used receiver array is sufficiently long, relative to the  
111 depth of the structure of interest, and given a sufficiently wide illumination (in terms of  
112 ray parameters and back azimuths), the autocorrelation in the GloPSI relation (1) can

113 be replaced by crosscorrelation, which would permit retrieval of offset reflections as  
114 well. This would allow for direct imaging of a broader range of dipping structures.

115 In Figure 1, we show in a schematic way how GloPSI would (or would not)  
116 retrieve reflection responses from four different structural settings.

117

### 118 **Comparison with the receiver-function method**

119 The receiver-function method depends on phase conversions (*P*-to-*S* or  
120 *S*-to-*P*) occurring in transmission. GloPSI with *P*-wave phases uses reflection  
121 information and depends only on the *P*-wave impedance contrasts, just like the  
122 conventional reflection method. Comparisons of imaging results from SI and receiver  
123 function have shown that SI provides images with resolution at least as high as the  
124 receiver-function image (Abe et al., 2007). In cases of structural contrasts that are due  
125 to relatively thin layers, SI has the potential to provide higher resolution than the  
126 receiver function. For example, suppose there is a mantle structure 5 km below the  
127 Moho, which is illuminated by a *P*-wave phase with an incidence angle of  $10^\circ$ . The *P*-  
128 and *S*-wave velocities between the structure and the Moho are 8.1 km/s and 4.5 km/s,

129 respectively, while above the Moho the respective velocities are 5 km/s and 2.5 km/s.  
130 The receivers at the surface would record the *P*-to-*S* converted waves from the two  
131 boundaries with a time difference of 0.49 s – the time difference for the propagation of  
132 the *P*- and *S*-waves between the mantle structure and the Moho. A virtual zero-offset  
133 reflection recording, retrieved from GloPSI, would contain two *P*-wave reflections  
134 from the impedance contrasts at the Moho and the mantle structure arriving with a time  
135 difference of 1.23 s. In terms of wavelength, assuming a center frequency for both *P*-  
136 and *S*-waves of 0.8 Hz, the two arrivals in the recordings used by the receiver-function  
137 method would be 0.39 wavelengths apart. In the retrieved recordings from GloPSI, the  
138 two *P*-wave reflections would be 0.99 wavelengths apart, which would allow for  
139 higher resolution.

140 Thus, although until now SI or GloPSI has not been applied for imaging of  
141 aseismic slab zones, these methods have the potential to image such zones with  
142 temporal (depth) resolution higher than the one that can be achieved using the  
143 receiver-function method.

144

145 **Data**

146 **Study area**

147           Figure 2 shows the location of intermediate-depth earthquakes that have  
148 occurred from August 1906 to July 2014 around the Malargüe region (35.5°S),  
149 Argentina. The locations are taken from the U.S. Geological Survey (USGS,  
150 <http://earthquake.usgs.gov/earthquakes/>) earthquake catalog. There could be more  
151 earthquakes actually present than we show in Figure 2 if they are not in the catalog.  
152 Note that there are no earthquakes deeper than around 200 km. There is also an  
153 aseismic spot beneath the Peteroa Volcano. This volcano forms part of the  
154 Planchón-Peteroa volcanic complex. We are interested in imaging these aseismic  
155 zones, and we achieve this using GloPSI. In Figure 2, the station GO05 of the Chilean  
156 National Seismic Network and the station C02A of the Talca Seismic Network, which  
157 we use later for quality-control purpose, are also plotted.

158

159 **MalARRgüe**

160           We apply GloPSI to data from the MalARRgüe array (Ruigrok et al., 2012).

161 The array recorded continuously ambient noise and seismicity during 2012 in the  
162 Malargüe region, Argentina, to the east of the southern part of central Chile. The array  
163 consisted of a patchy subarray PV and an exploration-style 2D T-shaped subarray T  
164 with arms TN and TE pointing north and east, respectively, see Figure 3. MalARRgüe  
165 used short-period (2-Hz) sensors borrowed from the Program for Array Seismic  
166 Studies of the Continental Lithosphere (PASSCAL) managed by Incorporated  
167 Research Institutions for Seismology (IRIS). The PV-array consisted of 6 irregularly  
168 spaced stations labeled PV01 to PV06; the TN-array formed a line of 19 stations  
169 spaced at 2 km and labeled TN02 to TN20, while the TE-array formed a line of 13  
170 stations spaced at 4 km and labeled TE01 to TE13.

171 Figure 3 shows the distribution of the global earthquakes we use to extract  
172 phases at the PV- and T-array, which phases are then used as input for GloPSI. The  
173 T-array lies above the beginning of the Nazca's aseismic zone, where possible slab  
174 tearing (Pesicek et al., 2012) and/or presence of plume decapitation (Burd et al., 2014)  
175 have been proposed.

176

177 **Selecting and extracting global phases**

178           We use the vertical-component recordings of the MalARRgue array for  
179 GloPSI. Using Java version of Windows Extracted from Event Data (JWEED) from  
180 IRIS and a reference earthquake catalogue from USGS, from the recorded total amount  
181 of global earthquakes with  $M_W \geq 5.5$ , we select 66, 72, and 85 earthquakes for the PV-,  
182 TN-, and TE-array, respectively (Table 1). We use *PKP*, *PKiKP* and *PKIKP* phases  
183 (epicentral distances  $\geq 120^\circ$ ), which travel through the mantle and core and arrive at  
184 the stations with absolute slowness  $< 0.04$  s/km (Kennett et al., 1995). We search the  
185 phases visually using a window of 900 s, which starts 100 s before the expected arrival  
186 of the specific *P*-wave phase; we also use as guides the phase pickings that are  
187 automatically calculated by IRIS. Then, we extract the desired phases from a shorter  
188 window, which is at least 200 s long. This window starts before the arrival of the  
189 specific *P*-wave phase and terminates before onset of the first *S*-wave phase. Figure 4  
190 shows an example of the windowing.

191           For quality control, as described below, we also use data from the station  
192 GO05 from the Chilean National Seismic Network, which is situated above the seismic

193 zone of the Nazca slab. For GO05, we use 52 earthquakes recorded by the station  
194 during the operation of MalARRgue (Table 1). The complete list of the used  
195 earthquakes for MalARRgue and GO05 is given in Table 1.

196

## 197 **Data Processing**

### 198 **Data processing for obtaining images**

199           After deconvolving the recordings with the instrument response, we  
200 compute power spectral densities (PSD) of the global-phase earthquakes to help us  
201 select a frequency band that provides adequate signal-to-noise ratio of the global  
202 phases. Figure 5 shows an example of the computed PSD for earthquakes of different  
203 magnitude higher than 5.5 that occurred at global distances. We select the band 0.3-1.0  
204 Hz using a 5<sup>th</sup>-order butterworth filter, as in this band all signals of the earthquakes are  
205 clearly observed (Figure 5). The lower limit of our band is set at 0.3 Hz due to the  
206 low-frequency limitations of the used instruments (Nishitsuji et al., 2014), as well as to  
207 make sure that the double-frequency microseisms noise is largely excluded.

208           After selecting the frequency band between 0.3 Hz and 1 Hz, we

209 downsample the data from the original sampling of 0.01 s to 0.25 s with the aim to  
210 minimize the volume of data. After that, we normalize each selected and filtered phase  
211 with respect to its maximum amplitude. We also apply despiking to trace intervals with  
212 very strong (accidental) signal spikes that saturate the trace for some time (the interval  
213 duration). For the TN- and TE-array, missing traces at certain stations (e.g., due to  
214 despiking) are interpolated using the corresponding records at their neighboring  
215 stations (Figure 6).

216           After the above preprocessing, we apply GloPSI to the selected events for  
217 each of the subarrays from MalARRgue (Figure 7). The retrieved zero-offset reflection  
218 trace at each station is dominated in the first few seconds by the average  
219 autocorrelation convolved with a delta function,  $\bar{E}_n(t) * \delta(t)$ . To suppress the effect of  
220  $\bar{E}_n(t)$ , for each subarray we extract the effective source time functions  $\bar{E}_n(t)$  from  
221 each retrieved zero-offset trace per subarray for a two-way travelttime from 0 to 10 s,  
222 take their mean, and subtract the mean from the individual traces in each subarray  
223 (Figure 8). This does not cause any changes to signals retrieved later than 10 s, while  
224 earlier than 10 s it preserves the differences between a trace and the mean. The

225 effective source time function of 10 s was selected after testing the above procedure for  
226 values from 8 s to 13 s with steps of 1 s.

227

### 228 **PKP triplication**

229 We also investigate the effect on our results of the *PKP* triplication (Adams  
230 and Randall, 1963) using the T-array. The *PKP* triplication is expected to arise for  
231 earthquakes at epicentral distances from about 135° to 155°. The triplicated arrivals are  
232 expected within 10 s from the first *PKP* arrival (e.g., Garcia et al., 2004). Each of the  
233 *PKP* triplications will contribute in the autocorrelation process to the retrieval of the  
234 same reflections (for example from the Moho) and thus would result in an increased  
235 signal-to-noise ratio of the reflections. For each transmission response, the individual  
236 *PKP* triplicated arrivals will also correlate with each other, which will result in the  
237 retrieval of artifacts in the result from each transmission response (cross-talk).  
238 However, according to the 3D theory of SI for any inhomogeneous medium, i.e., what  
239 we use here, such triplication-related artifacts will cancel out after summing over the  
240 correlated transmission responses (e.g., Wapenaar, 2003). Because of this, Ruigrok and

241 Wapenaar (2012) suggested using global phases from a wide range of ray parameters.  
242 In the summation process after the autocorrelation, this would cause the different  
243 cross-talk artifacts to interact destructively. This happens, as the cross-talk artifacts  
244 would be retrieved at different times. On the other hand, correlations of global phases  
245 with a wide azimuthal and slowness coverage enhance the physical arrivals, i.e., the  
246 signal-to-noise ratio of structures like Moho) is improved (Snieder, 2004). In our case,  
247 the azimuthal coverage and the slowness variation of the earthquakes with epicentral  
248 distances  $\geq 120^\circ$  are sufficiently wide (see Figure 3), so we did not exclude the  
249 earthquakes that would contain *PKP* triplications. To the contrary, if we exclude the  
250 epicentral distances causing *PKP* triplication, only 13 earthquakes would remain for  
251 both arms of the T-array from the original 72 and 85 earthquakes for the TN- and  
252 TE-array, respectively. A reduced number of used earthquakes would result in  
253 deterioration of the retrieved reflections from deeper structures.

254 In Figure 9, we show a comparison of the obtained images of the subsurface  
255 when including and excluding the *PKP* triplication. When the velocity model of  
256 Gilbert et al. (2006) is used for the depth conversion, the top of the Moho is interpreted

257 at a depth of 35 km, while the possible effect of the *PKP* triplication should be seen  
258 between depths of 35 km and 66 km. The comparison of the results in Figure 9 shows  
259 that the Moho in the results when earthquakes with triplications are included is well  
260 imaged without apparent large-amplitude “ringing” around it due to the *PKP*  
261 triplication. In our context, “large” means the amplitude as large as the one of the first  
262 Moho reflection, i.e., the reflection at around 30 km in Figure 9. There are some slight  
263 differences in the weaker-amplitude events (e.g., positive-amplitude waveforms about  
264 10 km after the Moho reflection), which we attribute to an insufficient integration over  
265 the small number of the earthquakes (only 13) when earthquakes with triplications are  
266 excluded. Note that the triplication “ringing” should be present also shallower than the  
267 Moho, but there it would be suppressed, even when present, by the subtraction of the  
268 averaged source time function  $\bar{E}_n(t)$ .

269         The same reasoning for the suppression of cross-talk due to *PKP* triplication  
270 is also valid for the suppression of source-side reverberations – due to differences in  
271 the source depths of the different earthquakes, the cross-talk in the autocorrelation  
272 between the transmission and the source-side reverberation would be suppressed when

273 summing over the different earthquakes due to destructively interference (Draganov et  
274 al., 2004, 2006).

275

### 276 **Predictive deconvolution and seismic migration**

277           The bottom of the sedimentary basin (top of basement) often causes  
278 relatively strong free-surface multiples (Hansen and Johnson, 1948). The depth of the  
279 Malargüe basin (a sub-basin in the Neuquén basin) below the T-array is known  
280 (Nishitsuji et al., 2014). This allows us to suppress the basement free-surface multiples  
281 by applying a predictive-deconvolution filter (Yilmaz, 1987) based on the estimated  
282 two-way travelttime of these multiples. Note that such a filter was not used for the  
283 PV-array, as it is not above a basin (Moscoso et al., 2011). After interpreting the Moho  
284 below each subarray following as guidance the interpretation by Gilbert et al. (2006),  
285 we also apply predictive-deconvolution filter for possible free-surface multiples from  
286 the Moho.

287           As the subsurface structures might not be planar below the subarrays,  
288 migration processing would be effective in moving dipping structures to their correct

289 location given an array has a sufficient length. In this study, we apply Kirchhoff  
290 post-stack time migration (Yilmaz, 1987) to the GloPSI sections from the TN- and  
291 TE-array. Migration is not applied for the PV-array due to its limited aperture; instead,  
292 the individual traces are stacked.

293         As final processing steps, we apply lateral smoothing along the array to aid  
294 the interpretation, using smoothed discretized splines based on the generalized  
295 cross-validation (Garcia, 2010) (Figure 10), and then convert the migrated or stacked  
296 traces from time to depth (Figure 11). For the depth conversion, we use a regional  
297 velocity model down to 70 km depth (Gilbert et al., 2006) and the ak135 model  
298 (Kennett et al., 1995) deeper than 70 km.

299         In Figure 10, we show a comparison of the obtained images when source  
300 time functions of 10 s and 12 s are used in the estimation of  $\bar{E}_n(t)$ . It can be seen that  
301 the different values give comparable results, which shows the robustness of the  
302 procedure. The only substantial difference between the images in Figure 10 is in the  
303 interpretation of the top of Moho. When using a two-way traveltime of 12 s, it seems  
304 that the Moho is largely removed due to its consistent depth over the subarrays.

305 Although it might be possible to improve the time window by taking into account  
306 individual source time functions, we found that the constant time window of 10 s is  
307 sufficiently effective as we do not see major differences with the result when using a  
308 window of 12 s. According to Kanamori and Brodsky (2004), the time window of 10 s  
309 covers source time functions for earthquakes smaller or equal to  $M_W$  6.5. Only 8% of  
310 the earthquakes used for the TN array has  $M_W > 6.5$ .

311 For the GO05 station, we apply the same processing as for the PV-array,  
312 except that during the depth conversion we apply the velocity model as used for the  
313 C02A station of the Talca Seismic Network in Dannowski et al. (2013) who utilized the  
314 velocity model of Bohm et al. (2002). An approximation of  $\bar{E}_n(t)$  is calculated by  
315 taking the average of the retrieved results for GO05 and stations GO04 and GO06,  
316 which are the N-S neighbors of GO05 in the Chilean National Seismic Network.

317

### 318 **Quality control of the results at the seismic zone of the Nazca slab**

319 For quality-control purpose, we first apply GloPSI to station GO05, which is  
320 situated above the seismic zone of the slab. In the processed traces, the peak and

321 trough of the wiggles correspond to depths of P-wave impedance contrasts. We  
322 compare the obtained GloPSI zero-offset reflection trace with the receiver-function  
323 trace obtained for C02A in Dannowski et al. (2013), see Figure 11a. From the  
324 receiver-function results, Dannowski et al. (2013) estimate the Moho depth at this  
325 location at 33 km. GloPSI for GO05 also shows strong amplitude around 33 km  
326 (Figure 11a). Note that around this depth starts a cluster of hypocenters (Figures 2 and  
327 11a). Hypocenter clustering delineates the slab, meaning that beneath GO05 the strong  
328 positive peaks at depths of about 40 km and 70 km correspond to the slab's top and  
329 bottom, respectively (dashed green lines in Figure 11a). The correspondence of the  
330 imaged reflectivity with the hypocenter clustering, but also with the slab's bottom from  
331 the receiver-function trace (second positive peak at C02A trace in Figure 11a) confirms  
332 the validity of applying GloPSI for slab imaging. Imaging reflectivity that is as strong  
333 as the Moho means, that below GO05 the slab is locally (nearly) flat (Figures 1a and  
334 1b). If the slab were locally inclined, the image would have exhibited lack of  
335 reflectivity (Figure 1c).

336

## 337 **Results Interpretation and Discussion**

### 338 **Aseismic spot beneath the Peteroa volcano (PV-array)**

339           Similar to the trace for station GO05, beneath the PV-array GloPSI reveals  
340 the Moho where the strongest amplitude is seen, that is at a depth of about 45 km  
341 (Figure 11b). This depth shows good agreement with a recent result of Gravity field  
342 and Ocean Circulation Explorer (GOCE) operated by European Space Agency (ESA,  
343 [www.esa.int/ESA](http://www.esa.int/ESA)) (e.g., Reguzzoni et al., 2013) that shows the Moho depth to be  
344 around 45 km in this region. A feature further down in the zero-offset reflection trace  
345 from the PV-array is the appearance of reflectivity packages at around 100 km and 150  
346 km depth, where the hypocenters of some intermediate-depth earthquake are present  
347 (Figure 11b). Another striking feature is the lack of reflectivity for about 15 km around  
348 the depth of 125 km. The latter corresponds to an aseismic spot at the Nazca slab.  
349 Because of the aseismicity and because GloPSI would not image structures where no  
350 impedance contrast exists (after applying predictive-deconvolution filter for possible  
351 free-surface multiples from the Moho), the lack of reflectivity might be interpreted as  
352 caused by certain amount of melt. If melted substance is indeed present around 125 km

353 depth, then one possible interpretation of the two strong-reflectivity packages at 100  
354 km and 150 km depth would be as reflections from slab deformation, which in turn  
355 would be caused by the melted substance. The deformation might be in the form of  
356 detachment, shearing, necking, or any combination thereof. We illustrate the three pure  
357 deformation scenarios in Figure 11d. The present hypocenters indicate vaguely the  
358 slab, which is generally characterized as steeply dipping in this zone. The dip would be  
359 too steep to retrieve reflections of a dipping interface delineating the slab (Figure 1c),  
360 but deformations at the slab would give rise to scattered energy. Some of this energy  
361 will be in the form of (nearly) vertically scattered fields, which will be recorded at the  
362 station (Figure 1d). The latter will be turned by GloPSI into zero-offset reflections, and  
363 consecutively imaged. If the slab is indeed deformed, depending on its thickness (e.g.,  
364 the transparent green ellipses in Figure 11d), the primary reflection from the top of the  
365 slab on one side of the deformation might interfere with the primary reflection from the  
366 bottom of the slab from the other side of the deformation, which would make the  
367 interpretation of the exact limits of the slab ambiguous. Because of this, in Figure 11b  
368 we indicate with dashed green lines only the extent of the possible deformation of the

369 slab. We interpret the bottom of the slab at around 175 km.

370           Note that if melt is present and forms an impedance contrast with the mantle  
371 and/or the slab, GloPSI would retrieve a reflection from this contrast as well unless the  
372 melt itself forms a steeply dipping structure (Yilmaz, 1987). However, if there is no or  
373 only weak impedance contrast due to, for example, the gabbro-eclogite transformation  
374 of the slab, GloPSI will not retrieve a clear reflection from the melt. Frank et al. (2014)  
375 showed that SI could be applied to *S*-wave phases as well (e.g., *S*, *SS*, *ScS*, and *SKS*).  
376 *S*-waves have the advantage that they are more sensitive to melt than *P*-waves and thus  
377 can provide extra information. An implementation of GloPSI to *S*-wave phases would  
378 entail the use of global phases like *PKS* and *SKS*. Such implementation to our  
379 temporary deployment would be challenging due to the low signal-to-noise ratio on the  
380 horizontal components and the attenuation of much of the *S*-wave phases below the  
381 sensitivity bandwidth of the instruments.

382           We do not exclude other possible interpretations for the lack of reflectivity  
383 around 125 km. However, our interpretation is a logical consequence of the presence of  
384 only a few intermediate-depth earthquakes: the slab here is insufficiently brittle to

385 generate many earthquakes and that might be indicative of a presence of magma with  
386 possible slab deformation. Our interpretation is in a good agreement with results from  
387 recent geochemical investigations of Jacques et al. (2013) suggesting that the  
388 Planchón-Peteroa complex erupts not only lithospheric magma from the heterogeneous  
389 mantle, but also magma from the Nazca slab.

390

391 **Aseismic zone of the Nazca slab beneath the T-array**

392 The migrated images obtained from the results retrieved from GloPSI  
393 beneath the TN- and TE-arrays are shown in Figure 11c. With the receiver-function  
394 method, Gilbert et al. (2006) interpreted an apparently bifurcated Moho, with possibly  
395 a magma chamber in between, to be present in this region. Our result shows two strong  
396 positive peaks, which appears to confirm the observation of Gilbert et al. (2006). Based  
397 on their interpretation, we label the Moho and the magma chamber in Figure 11c where  
398 the trough in blue is imaged at a depth of about 40 km. Our GloPSI image shows that  
399 the bifurcation is continuous beneath the TN-array, but wedges out to the east beneath  
400 the TE-array.

401           The image of the upper mantle beneath both arms of the T-array reveals a  
402 complex structure. This heterogeneous image might correspond to the interpretation of  
403 the study of Jacques et al. (2013). In their study, the authors indicated that the mantle  
404 wedge in this region seems to be characterized, from a point of view of geochemical  
405 components, by crustal assimilation or mantle heterogeneity. Note that if non-primary  
406 reflections and spurious phases from autocorrelation cross-talk are retrieved, they will  
407 contribute to the apparent complexity of the structure. The latter could be caused by  
408 source-side reflections (even though we expect such cross-talk to be suppressed by the  
409 summation over the different earthquakes), micro-seismic noise, etc.

410           Below 100 km, we notice a pronounced discontinuity of the imaged  
411 reflectors, indicated by the dashed green line in Figure 11c. This discontinuity is  
412 clearly observed below the TE-array from the middle of the array (100 km depth)  
413 towards the east (150 km depth). Due to the limited aperture of the T-array, deeper  
414 steeply dipping structures will not be imaged, but will manifest themselves as lack of  
415 reflectivity (Figure 4-43 in Yilmaz, 1987). For instance, to record the free-surface  
416 multiple of the vertically incident global phase after it is reflected from the Nazca slab

417 characterized by a dip of  $40^\circ$  and depth of 200 km, we need a receiver at the free  
418 surface with an offset from the virtual-source position of more than 1000 km (Figure  
419 1c). This can also be said in another way: to retrieve zero-offset reflection from a  
420 structure with a dip of  $40^\circ$ , we will need to record incoming phases with incidence  
421 angle of  $40^\circ$  as well, which is not possible with global phases. Although some  
422 reflection discontinuities may be seen shallower than 150 km, it is difficult to interpret  
423 them without other geophysical information. Note that a longer seismic array would be  
424 required to better interpret the mantle structure. Since there is a possible remnant of an  
425 upwelling plume in this region (Burd et al., 2014), some of these discontinuities might  
426 be related to the plume, but they might also be related to a part of the mantle  
427 convection or partial melting.

428         Let us look at the deeper part of the GloPSI image, where, based on the  
429 extrapolation of the mapped hypocenters, we expect to see the Nazca slab. A  
430 dimmed-reflectivity zone (between the dashed green lines) is visible beneath the  
431 TN-array dipping from NNW around a depth of 180 km to 200 km to the SSE. This  
432 zone causes discontinuity in the strong laterally coherent horizons A and B in Figure

433 11c. Beneath the TE-array, the GloPSI image exhibits a clear dimmed-reflectivity zone  
434 (between the dashed green lines) dipping with an angle of  $43^\circ$  to the east and causing  
435 discontinuity in horizon B. Note that horizon B is also visible around 62.5 s in Figure  
436 10. The dimmed reflectivity might be caused by lack of impedance contrasts. This,  
437 though, would not result in discontinuity of the imaged reflectors. As explained above,  
438 another reason for the dimmed reflectivity might be the presence of dipping reflectors,  
439 which, because of their depth and the relatively short array length, would not be well  
440 imaged in the (migrated) section (Yilmaz, 1987). The presence of such dipping  
441 reflectors would be manifested by discontinuity in horizontal reflectors (Figure 11c).  
442 That is why, we interpret this dipping dimmed-reflectivity zone as the top and bottom  
443 of the aseismic zone of the Nazca slab. We see that this part of the interpreted slab is  
444 continuous and that the reflectivity does not indicate a possible slab deformation at this  
445 latitude ( $35.5^\circ\text{S}$ ). Since there is no seismicity along this part of the slab, the condition  
446 of this steeply dipping slab zone might be different from the condition in the shallower  
447 zone where seismicity is present. This might support the interpretation of Yuan et al.  
448 (2000) who proposed a completion of the eclogite transformation along this part of the

449 slab.

450

## 451 **Conclusions**

452           We presented seismic interferometry with global phases (GloPSI) for  
453 imaging the aseismic and seismic parts of a subducting slab and the mantle above it.  
454 GloPSI retrieves reflection responses from coinciding virtual source and receiver at  
455 each seismic station to which it is applied. We applied the method to global P-wave  
456 phases recorded by an array of short-period stations installed for one year in the  
457 Malargüe region, Argentina, located east of the southern part of central Chile. The  
458 array consisted of a station distribution to the east of the Peteroa volcano and two  
459 linear subarrays to the east of the town of Malargüe. We processed the retrieved  
460 reflection responses to obtain depth images of the subsurface beneath the array. The  
461 images to the east of Malargüe town revealed, with high horizontal and vertical  
462 resolution, a bifurcated Moho and a complex-structured upper mantle. On the images,  
463 we also interpreted the aseismic part of the Nazca slab, which manifested itself as  
464 dimmed reflectivity due to the relation between the depth of the dipping reflectors and

465 the short array length we used. The aseismic part of the slab appears to be without tears  
466 and to be dipping with an angle of  $43^\circ$  to the east. The image beneath Peteroa also  
467 showed the Moho. The deeper part of the image shows packages of strong reflectivity  
468 with lack of reflectivity between them. These might be interpreted as a deformation in  
469 the dipping slab. If so, the interpreted deformation could be in the form of detachment,  
470 shearing, necking, or any combination thereof.

471

## 472 **Acknowledgements**

473 The data used in this study are collected using Java version of Windows Extracted  
474 from Event Data (JWEED) of Incorporated Research Institutions for Seismology  
475 (IRIS, <http://www.iris.edu/dms/nodes/dmc/>) and a reference earthquake catalogue from  
476 U.S. Geological Survey (USGS, <http://earthquake.usgs.gov/earthquakes/>). This  
477 research is supported by the Division for Earth and Life Sciences (ALW) with financial  
478 aid from the Netherlands Organization for Scientific Research (NWO) with grant VIDI  
479 864.11.009. The research of E.R. and K.W. was supported by the Netherlands Research  
480 Centre for Integrated Solid Earth Sciences (ISES). The authors thank IRIS-PASSCAL

481 for providing the seismic equipment and the Argentine Ministry of Science,  
482 Technology and Production Innovation for the financial support connected to the  
483 transportation of the equipment. The authors also thank Pierre Auger Observatory and  
484 the department of Civil Defense of Malargüe for the help during the data acquisition.  
485 The authors are thankful to Issei Doi at Kyoto University for a discussion. The authors  
486 thank Nori Nakata at Stanford University for his constructive comments on an earlier  
487 version of the manuscript. The authors also thank Sjoerd de Ridder, the assistant  
488 special editor, and two anonymous reviewers for their constructive comments that  
489 improved the quality of this manuscript. The maps were drawn with  
490 GenericMappingTool (GMT) (Wessel and Smith, 1991).

491

## 492 **References**

- 493 Abe, S., E. Kurashimo, H. Sato, N. Hirata, T. Iwasaki, and T. Kawanaka, 2007,  
494 Interferometric seismic imaging of crustal structure using scattered teleseismic  
495 waves: Geophysical Research Letters, **34**, L 19305, doi: 10.1029/2007GL030633.
- 496 Adams, R. D., and M. J. Randall, 1963, Observed triplication of PKP: Nature, **200**,

- 497 744-745, doi: 10.1038/200744a0.
- 498 Audet, P., M. G. Bostock, N. I. Christensen, and S. M. Peacock, 2009, Seismic evidence  
499 for overpressured subducted oceanic crust and megathrust fault sealing: *Nature*,  
500 **457**, 76-78, doi: 10.1038/nature07650.
- 501 Aki, K., A. Christoffersson, and E. S. Husebye, 1977, Determination of the  
502 three-dimensional seismic structure of the lithosphere: *Journal of Geophysical*  
503 *Research*, **82**, 277-296, doi: 10.1029/JB082i002p00277.
- 504 Anderson, M., P. Alvarado, G. Zandt, and S. Beck, 2007, Geometry and brittle  
505 deformation of the subducting Nazca Plate, Central Chile and Argentina:  
506 *Geophysical Journal International*, **171**, 419-434, doi:  
507 10.1111/j.1365-246X.2007.03483.x.
- 508 Becker, J. J., D. T. Sandwell, W. H. F. Smith, J. Braud, B. Binder, J. Depner, D. Fabre,  
509 J. Factor, S. Ingalls, S. H. Kim, R. Ladner, K. Marks, S. Nelson, A. Pharaoh, R.  
510 Trimmer, J. Von Rosenberg, G. Wallace, and P. Weatherall, 2009, Global  
511 bathymetry and elevation data at 30 arc seconds resolution: SRTM30\_PLUS:  
512 *Marine Geodesy*, **32**, 355–371, doi: 10.1080/01490410903297766.

- 513 Bloch, W., J. Kummerow, P. Salazar, P. Wigger, and S. A. Shapiro, 2014,  
514 High-resolution image of the North Chilean subduction zone: seismicity,  
515 reflectivity and fluids: *Geophysical Journal International*, **197**, 1744–1749, doi:  
516 10.1093/gji/ggu084.
- 517 Bohm, M., S. Lüth, H. Echtler, G. Asch, L. Bataille, C. Bruhn, A. Rietbrock, and P.  
518 Wigger, 2002, The Southern Andes between 36° and 40° S latitude: seismicity and  
519 average seismic velocities: *Tectonophysics*, **356**, 275-289, doi:  
520 10.1016/S0040-1951(02)00399-2.
- 521 Booker, J. R., A. Favetto, and M. C. Pomposiello, 2004, Low electrical resistivity  
522 associated with plunging of the Nazca flat slab beneath Argentina: *Nature*, **429**,  
523 399-403, doi: 10.1038/nature02565.
- 524 Boschi, L., and T. W. Becker, 2011, Vertical coherence in mantle heterogeneity from  
525 global seismic data: *Geophysical Research Letters*, **39**, L20306, doi:  
526 10.1029/2011GL049281.
- 527 Burd, A. I., J. R. Booker, R. Mackie, A. Favetto, and M. C. Pomposiello, 2014,  
528 Three-dimensional electrical conductivity in the mantle beneath the Payún Matrú

- 529 Volcanic Field in the Andean backarc of Argentina near 36.5°S: evidence for  
530 decapitation of a mantle plume by resurgent upper mantle shear during slab  
531 steepening: *Geophysical Journal International*, **198**, 812-827, doi:  
532 10.1093/gji/ggu145.
- 533 Cahill, T., and B. Isacks, 1992, Seismicity and shape of the subducted Nazca plate:  
534 *Journal of Geophysical Research*, **97**, 17503-17529, doi: 10.1029/92JB00493.
- 535 Claerbout, J., 1968, Synthesis of a layered medium from its acoustic transmission  
536 response: *Geophysics*, **33**, 264-269, doi: 10.1190/1.1439927.
- 537 Daneshvar, N. R., C. S. Clay, and M. K. Savage, 1995, Passive seismic imaging using  
538 microearthquakes: *Geophysics*, **60**, 1178-1186, doi: 10.1190/1.1443846.
- 539 Dannowski, A., I. Grevemeyer, H. Kraft, I. Arroyo, and M. Thorwart, 2013, Crustal  
540 thickness and mantle wedge structure from receiver functions in the Chilean  
541 Maule region at 35°S: *Tectonophysics*, **592**, 159-164, doi:  
542 10.1016/j.tecto.2013.02.015.
- 543 Draganov, D., K. Wapenaar, and J. Thorbecke, 2004, Passive seismic imaging in the  
544 presence of white noise sources: *The Leading Edge*, **23**, 889–892, doi:

- 545        10.1190/1.1803498.
- 546    Draganov, D., K. Wapenaar, and J. Thorbecke, 2006, Seismic interferometry:  
547        reconstructing the Earth's reflection response: *Geophysics*, **71**, SI61–SI70, doi:  
548        10.1190/1.2209947.
- 549    Dziewonski, A. M., B. H. Hager, and R. J. O'Connell, 1977, Large-scale  
550        heterogeneities in the lower mantle: *Journal of Geophysical Research*, **82**, 239-255,  
551        doi: 10.1029/JB082i002p00239.
- 552    Eakin, C. M., M. D. Long, S. L. Beck, L. S. Wagner, H. Tavera, and C. Condori, 2014,  
553        Response of the mantle to flat slab subduction: insights from local S splitting  
554        beneath Peru: *Geophysical Research Letters*, **41**, 3438-3446, doi:  
555        10.1002/2014GL059943.
- 556    Frank, J. G., E. N. Ruigrok, and K. Wapenaar, 2014, Shear wave seismic interferometry  
557        for lithospheric imaging: application to southern Mexico: *Journal of Geophysical*  
558        *Research*, **119**, 5713-5726, doi: 10.1002/2013JB010692.
- 559    Garcia, D., 2010, Robust smoothing of gridded data in one and higher dimensions with  
560        missing values: *Computational Statistics and Data Analysis*, **54**, 1167-1178, doi:

- 561        10.1016/j.csga.2009.09.020.
- 562        Garcia, R., S. Chevrot, and M. Webber, 2004, Nonlinear waveform and delay time  
563        analysis of triplication core phases: *Journal of Geophysical Research*, **109**,  
564        B01306, doi: 10.1029/2003JB002429.
- 565        Gilbert, H., S. Beck, and G. Zandt, 2006, Lithospheric and upper mantle structure of  
566        central Chile and Argentina: *Geophysical Journal International*, **165**, 383–398,  
567        doi: 10.1111/j.1365-246X.2006.02867.x.
- 568        Hansen, R. F., and C. H. Johnson, 1948, Multiple reflections of seismic energy:  
569        *Geophysics*, **13**, 58-85, doi: 10.1190/1.1437377.
- 570        Jacques, G., K. Hoernle, J. Gill, F. Hauff, H. Wehrmann, D. Garbe-Schönberg, P. van  
571        den Bogaard, I. Bindeman, and L. E. Lara, 2013, Across-arc geochemical  
572        variations in the Southern Volcanic Zone, Chile (34.5-38.0°S): constraints on  
573        mantle wedge and slab input compositions: *Geochimica et Cosmochimica Acta*,  
574        **123**, 218-243, doi: 10.1016/j.gca.2013.05.016.
- 575        Kanamori, H., and E. E. Brodsky, 2004, The physics of earthquakes: Reports on Progress  
576        in Physics, **67**, 1429-1496, doi: 10.1088/0034-4885/67/8/R03.

- 577 Kawakatsu, H., and S. Yoshioka, 2011, Metastable olivine wedge and deep dry cold slab  
578 beneath southwest Japan: *Earth and Planetary Science Letters*, **303**, 1-10, doi:  
579 10.1016/j.epsl.2011.01.008.
- 580 Kennett, B. L. N., E. R. Engdahl, and R. Buland, 1995, Constraints on seismic  
581 velocities in the earth from travel times: *Geophysical Journal International*, **122**,  
582 108–124, doi: 10.1111/j.1365-246X.1995.tb03540.x.
- 583 Kumar, M. R., and M. G. Bostock, 2006, Transmission to reflection transformation of  
584 teleseismic wavefields: *Journal of Geophysical Research*, **111**, B08306, doi:  
585 10.1029/2005JB004104.
- 586 Langston, C. A., 1979, Structure under Mount Rainier, Washington, inferred from  
587 teleseismic body waves: *Journal of Geophysical Research*, **84**, 4749-4762, doi:  
588 10.1029/JB084iB09p04749.
- 589 Moscoso, E., I. Grevemeyer, E. Contreras-Reyes, E. R., Flueh, Y. Dzierma, W. Rabbel,  
590 and M. Thorwart, 2011, Revealing the deep structure and rupture plane of the  
591 2010 Maule, Chile earthquake( $M_w$ 8.8) using wide angle seismic data: *Earth and*  
592 *Planetary Science Letters*, **307**, 147-155, doi: 10.1016/j.epsl.2011.04.025.

- 593 Nishitsuji, Y., E. Ruigrok, M. Gomez, and D. Draganov, 2014, Global-phase H/V  
594 spectral ratio for delineating the basin in the Malargüe region, Argentina:  
595 Seismological Research Letters, **85**, 1004-1011, doi: 10.1785/0220140054.
- 596 Nowack, R. L., S. Dasgupta, G. T. Schuster, and J. M. Sheng, 2006, Correlation migration  
597 using Gaussian beams of scattered teleseismic body waves: Bulletin of the  
598 Seismological Society of America, **96**, 1-10, doi: 10.1785/0120050036.
- 599 Pesicek, J. D., E. R. Engdahl, C. H. Thurber, H. R. DeShon, and D. Lange, 2012,  
600 Mantle subduction slab structure in the region of the 2010 M8.8 Maule earthquake  
601 (30-40°S), Chile: Geophysical Journal International, **191**, 317–324, doi:  
602 10.1111/j.1365-246X.2012.05624.x.
- 603 Reguzzoni, M., D. Sampietro, and F. Sansò, 2013, Global Moho from the combination of  
604 the CRUST2.0 model and GOCE data: Geophysical Journal International, **195**,  
605 222–237, doi: 10.1093/gji/ggt247.
- 606 Rosenbaum, G., D. Giles, M. Saxon, P. G. Betts, R. Weinberg, and C. Duboz, 2005,  
607 Subduction of the Nazca ridge and the Inca plateau: insights into the formation of  
608 ore deposits in Peru: Earth and Planetary Science Letters, **239**, 18-32, doi:

609 10.1016/j.epsl.2005.08.003.

610 Ruigrok, E., X. Campman, D. Draganov, and K. Wapenaar, 2010, High-resolution  
611 lithospheric imaging with seismic interferometry: Geophysical Journal  
612 International, **183**, 339–357, doi: 10.1111/j.1365-246X.2010.04724.x.

613 Ruigrok, E., and K. Wapenaar, 2012, Global-phase seismic interferometry unveils  
614 P-wave reflectivity below the Himalayas and Tibet: Geophysical Research  
615 Letters, **39**, L11303, doi: 10.1029/2012GL051672.

616 Ruigrok, E., D. Draganov, M. Gomez, J. Ruzzante, D. Torres, I. Lopes Pumarega, N.  
617 Barbero, A. Ramires, A. R. Castano Ganan, K. van Wijk, and K. Wapenaar,  
618 2012, Malargüe seismic array: design and deployment for the temporary array:  
619 The European Physical Journal Plus, **127**, 126, doi: 10.1140/epjp/i2012-12126-7.

620 Scherbaum, F., 1987a, Seismic imaging of the site response using microearthquake  
621 recordings. Part I. Method: Bulletin of the Seismological Society of America, **77**,  
622 1905-1923.

- 623 Scherbaum, F., 1987b, Seismic imaging of the site response using microearthquake  
624 recordings. Part II. Application to the Swabian Jura southwest Germany, Seismic  
625 network: Bulletin of the Seismological Society of America, **77**, 1924-1944.
- 626 Snieder, R., 2004, Extracting the Green's function from the correlation of coda waves: a  
627 derivation based on stationary phase: Physical Review E, **69**, 046610, doi:  
628 10.1103/PhysRevE.69.046610.
- 629 Syracuse, E. M., and G. A. Abers, 2009, Systematic biases in subduction zone  
630 hypocenters: Geophysical Research Letters, **36**, L10303, doi:  
631 10.1029/2009GL037487.
- 632 Wapenaar, K., 2003, Synthesis of an inhomogeneous medium from its acoustic  
633 transmission response: Geophysics, **68**, 1756-1759, doi: 10.1190/1.1620649.
- 634 Wessel, P., and W. H. F. Smith, 1991, Free software helps map and display data: EOS  
635 Transactions AGU, **72**, 441-448, doi: 10.1029/90EO00319.
- 636 Wortel, M. J. R., and W. Spakman, 2000, Subduction and slab detachment in the  
637 Mediterranean-Carpathian region: Science, **290**, 1910-1917, doi:  
638 10.1126/science.290.5498.1910.

639 Yilmaz, Ö., 1987, Seismic data analysis: SEG.

640 Yuan, X., S. V. Sobolev, R. Kind, O. Oncken, G. Bock, G. Asch, B. Schurr, F. Graeber,

641 A. Rudloff, W. Hanka, K. Wylegalla, R. Tibi, Ch. Haberland, A. Rietbrock, P.

642 Giese, P. Wigger, P. Röwer, G. Zandt, S. Beck, T. Wallace, M. Pardo, and D.

643 Comte, 2000, Subduction and collision processes in the Central Andes constrained

644 by converted seismic phases: Nature, **408**, 958-961, doi: 10.1038/35050073.

645

646 **Figure captions**

647 Figure 1. : A schematic illustration of how GloPSI would or would not retrieve

648 reflection responses for: (a) a horizontally layered structure and vertical

649 transmission responses; (b) a gently dipping structure and nearly vertical

650 transmission responses; (c) as in (b), but for a steeply dipping structure; (d)

651 as in (c), but when an abrupt change (e.g., slab deformation) presents in

652 present in the lateral continuation of the dipping structure. The black lines

653 indicate the transmission response from the global earthquakes, while the

654 gray dashed lines depict the reflection response that will not be recorded at

655 the station due to the configuration. Two-way arrows indicate the  
656 reflection response that will be recorded at the station.

657 Figure 2. : Center – Location of the seismic stations used in our study, and hypocenters  
658 mapping using earthquakes archived by USGS. Below and right – distribution  
659 of the hypocenters in depth within the red dashed-line areas in NWW-SEE and  
660 NNE-SSW direction.

661 Figure 3. : Distribution of the global-phase earthquakes used in our study. The circles  
662 show the location of the earthquakes used for MalARRgue and the GO05  
663 station. The location of MalARRgue is indicated by the black triangle with  
664 its topography maps (Becker et al., 2009) in the insets. The distribution of  
665 the back azimuth of the earthquakes for the T-array is shown in the inset.

666 Figure 4. : An example recording of a global earthquake on the vertical component of  
667 the stations from the TN-array. The area highlighted in light blue indicates  
668 the used window that contains the global phases. The orange and green  
669 lines indicate the P- and S-wave phase onsets by IRIS, respectively.

670 Figure 5. : The computed power spectral densities for four earthquakes with different

671 magnitudes that occurred at global distances. The densities are computed  
672 for station TE01 of the TE-array in MalARRgue.  $\Delta$  indicates the  
673 epicentral distances of the global earthquakes.

674 Figure 6. : Number of original and interpolated global phases for TN- (top) and  
675 TE-array (bottom) stations.

676 Figure 7. : GloPSI results retrieved at the MalARRgue stations before seismic  
677 processing. The annotations along the horizontal axis show the actual  
678 station codes.

679 Figure 8. : The results from Figure 7 after subtraction of the mean  $\bar{E}_n(t)$  per subarray.

680 Figure 9. : A comparison of GloPSI images obtained when including and when  
681 excluding global phases with *PKP* triplications. The number of  
682 earthquakes for the TN(TE)-array with and without the *PKP* triplications  
683 are 72 (85) and 13 (13), respectively.

684 Figure 10. : GloPSI results for the TN- and TE-array after post-stack time migration  
685 with lateral smoothing in the offset orientation when respective source  
686 time functions of 10 s and of 12 s are used in the estimation of  $\bar{E}_n(t)$ .

687 Figure 11. : Summarized interpretation with seismicity along the NWW-SEE area of  
688 GloPSI for MalARRgue and station GO05. **a.** GloPSI for GO05 and  
689 receiver function for C02A at the Nazca-slab seismic zone. Moho depth is  
690 interpreted using receiver function (modified from Dannowski et al., 2013)  
691 at C02A. **b.** GloPSI for the PV-array beneath the Peteroa Volcano. **c.**  
692 GloPSI for the TN- and TE-array at the Nazca-slab aseismic zone. Dashed  
693 green lines in the panels indicate where we interpret the Nazca slab and  
694 transparent green rectangles indicate possible interval of the interpretation.  
695 The transparent green ellipses indicate where we interpret the Nazca-slab  
696 deformation, while the transparent gray triangle – the possible connection  
697 between the Nazca-slab seismic and aseismic zones in three dimensions.  
698 The insets in the bottom left corner illustrate three possible scenarios  
699 explaining the retrieved strong reflectivity below the PV-array. Gray  
700 circles (some transparent for visibility purposes) indicate earthquake  
701 hypocenters.

**Table 1.** Global-phase seismic used in this study

Date (month/d/yr)	Time (hr:min:s)	Lat. (°N)	Lon. (°E)	Dep. (km)	$M_w$	Array ID
01/18/12	12:50:21	-0.877	126.829	19	5.7	TE
01/28/12	0:17:11	13.386	124.586	35	5.5	TE
02/04/12	13:09:23	11.872	125.754	12	5.8	PV/TN/TE/GO
02/06/12	3:49:13	9.999	123.206	11	6.7	TE
02/06/12	4:20:00	10.092	123.227	10	5.6	TE
02/06/12	10:10:20	9.885	123.095	9	6.0	PV/TN/TE/GO
02/06/12	11:33:37	9.821	123.080	15	5.9	PV/TN/TE/GO
02/14/12	6:22:01	36.214	141.386	28	5.8	PV/TN/TE/GO
02/26/12	2:35:01	22.661	120.891	28	5.9	TE
02/26/12	6:17:20	51.708	95.991	12	6.6	PV/TN/TE/GO
02/29/12	14:32:48	35.200	141.001	26	5.6	TE
03/08/12	22:50:08	39.383	81.307	38	5.9	TE
03/12/12	6:06:41	36.741	73.152	11	5.7	PV/TN/TE
03/12/12	12:32:46	45.239	147.609	110	5.6	PV/TN/TE
03/14/12	9:08:35	40.887	144.944	12	6.9	PV/TN/TE
03/14/12	10:49:25	40.781	144.761	10	6.1	PV/TN/TE
03/14/12	12:05:05	35.687	140.695	10	6.0	PV/TN/TE
03/16/12	7:58:02	10.037	125.633	18	5.8	PV/TN/TE/GO
03/22/12	0:21:37	3.513	125.859	117	5.6	TE
03/27/12	11:00:45	39.859	142.017	15	6.0	PV/TN/TE/GO
04/01/12	14:04:25	37.116	140.957	48	5.8	PV/TN/TE
04/11/12	8:38:37	2.327	93.063	20	8.6	PV/TN/TE/GO
04/11/12	10:43:11	0.802	92.463	25	8.2	PV/TN/TE/GO
04/13/12	10:10:01	36.988	141.152	11	5.7	PV/TN/TE/GO
04/14/12	15:13:14	49.380	155.651	90	5.6	TE
04/15/12	5:57:40	2.581	90.269	25	6.3	PV/TN/TE/GO
04/20/12	22:19:47	3.256	93.853	25	5.8	TE
04/20/12	22:28:59	3.269	93.821	22	5.8	PV/TN/TE/GO
04/20/12	23:14:31	2.158	93.360	28	5.9	PV/TN/TE/GO
04/21/12	1:16:53	-1.617	134.276	16	6.7	PV/TN/TE/GO
04/23/12	21:21:45	0.374	125.293	48	5.7	TE/GO
04/23/12	22:40:22	48.397	154.739	31	5.7	PV/TN/TE
04/24/12	14:57:10	8.868	93.949	14	5.6	PV/TN/TE/GO
04/25/12	7:42:23	9.011	93.945	9	5.9	PV/TN/TE/GO
04/29/12	8:09:04	2.704	94.509	14	5.7	PV/TN/TE/GO
04/29/12	10:28:52	35.596	140.349	44	5.8	PV/TN/TE/GO
05/12/12	23:28:44	38.612	70.354	10	5.7	PV/TN/TE/GO
05/23/12	15:02:25	41.335	142.082	46	6.0	PV/TN/TE
06/05/12	19:31:34	34.943	141.132	15	6.1	PV/TN/TE
06/09/12	14:23:20	48.851	154.852	49	5.5	TE
06/09/12	21:00:18	24.572	122.248	70	5.9	PV/TN/TE
06/11/12	5:29:12	36.023	69.351	16	5.7	TE
06/14/12	20:17:25	1.293	126.828	61	5.5	TE
06/15/12	1:14:08	5.719	126.354	41	5.7	PV/TN/TE/GO
06/16/12	22:18:47	15.593	119.563	28	5.9	PV/TN/TE/GO
06/17/12	20:32:21	38.919	141.831	36	6.3	PV/TN/TE/GO
06/23/12	4:34:53	3.009	97.896	95	6.1	PV/TN/TE/GO
06/29/12	21:07:34	43.433	84.700	18	6.3	PV/TN/TE/GO
07/08/12	11:33:03	45.497	151.288	20	6.0	PV/TN/TE
07/11/12	2:31:17	45.401	151.424	10	5.7	PV/TN/TE
07/12/12	12:51:59	45.452	151.665	12	5.7	TE
07/12/12	14:00:34	36.527	70.906	198	5.8	PV/TN/TE
07/19/12	7:36:35	37.248	71.375	98	5.6	PV/TN/TE/GO
07/20/12	3:40:12	49.506	155.599	15	5.5	TE
07/20/12	6:10:25	49.407	155.907	19	6.0	PV/TN/TE/GO
07/20/12	6:32:56	49.354	156.132	10	5.9	PV/TN/GO
07/25/12	0:27:45	2.707	96.045	22	6.4	PV/TN/GO
08/11/12	12:23:18	38.329	46.826	11	6.5	TE
08/11/12	12:34:36	38.389	46.745	12	6.4	TE
08/12/12	10:47:06	35.661	82.518	13	6.2	PV/TN/TE/GO
08/14/12	2:59:38	49.800	145.064	583	7.7	PV/TN/TE
08/18/12	9:41:52	-1.315	120.096	10	6.3	PV/TN/TE
08/18/12	15:31:40	2.645	128.697	10	5.8	TE
08/25/12	14:16:17	42.419	142.913	55	5.9	PV/TN/TE/GO
08/26/12	15:05:37	2.190	126.837	91	6.6	PV/TN/TE/GO
08/29/12	19:05:11	38.425	141.814	47	5.5	PV/TN/TE/GO
08/31/12	12:47:33	10.811	126.638	28	7.6	PV/TN/TE/GO
08/31/12	23:37:58	10.388	126.719	40	5.6	PV/TN/TE/GO
09/03/12	6:49:50	6.610	123.875	12	5.9	PV/TN/TE/GO
09/03/12	18:23:05	-10.708	113.931	14	6.3	PV/TN/GO
09/03/12	19:44:22	7.905	125.044	10	5.7	PV/TN/TE/GO
09/08/12	6:54:19	21.527	145.923	5	5.6	TE
09/08/12	10:51:44	-3.177	135.109	21	6.1	PV/TN/GO
09/09/12	5:39:37	49.247	155.750	31	5.9	TE
09/11/12	1:28:19	45.335	151.111	14	5.5	PV/TN/TE/GO
09/11/12	16:36:50	11.838	143.218	8	5.9	TE
09/14/12	4:51:47	-3.319	100.594	19	6.3	PV/TN/GO
10/01/12	22:21:46	39.808	143.099	15	6.0	PV/TN
10/08/12	11:43:31	-4.472	129.129	10	6.2	PV/TN/GO
10/12/12	0:31:28	-4.892	134.030	13	6.6	PV/TN/GO
10/14/12	9:41:59	48.308	154.428	35	5.8	PV/TN
10/16/12	12:41:26	49.618	156.438	81	5.6	PV/TN
10/17/12	4:42:30	4.232	124.520	326	6.0	PV/TN
11/01/12	23:37:18	1.229	122.105	35	5.5	TE
11/02/12	18:17:33	9.219	126.161	37	6.1	TN/TE/GO
11/05/12	4:30:27	37.791	143.610	19	5.6	TN/TE/GO
11/06/12	1:36:22	1.374	122.200	25	5.6	TN/TE/GO
11/06/12	1:42:26	1.357	122.167	35	5.6	TE
11/11/12	1:12:39	23.005	95.885	14	6.8	TN/TE/GO
11/14/12	5:21:42	9.982	122.472	41	5.7	TN/TE/GO
11/16/12	18:12:40	49.280	155.425	29	6.5	TN/TE/GO
11/27/12	7:34:25	17.684	145.763	192	5.5	TE
12/07/12	8:18:23	37.890	143.949	31	7.3	PV/TN/TE/GO
12/09/12	21:45:35	6.703	126.166	63	5.8	PV/TN/TE/GO
12/10/12	16:53:09	-6.533	129.825	155	7.1	PV/TN/GO
12/11/12	6:18:27	0.533	126.231	30	6.0	PV/TN/TE
12/17/12	9:16:31	-0.649	123.807	44	6.1	PV/TN/TE

Date, Time, Lat., Lon., Dep. and  $M_w$ , the moment magnitude, are provided by USGS (<http://earthquake.usgs.gov/earthquakes/>). For Array

ID, PV, TE, TN, and GO indicate PV-array, TE-array, TN-array, and GO05, respectively.

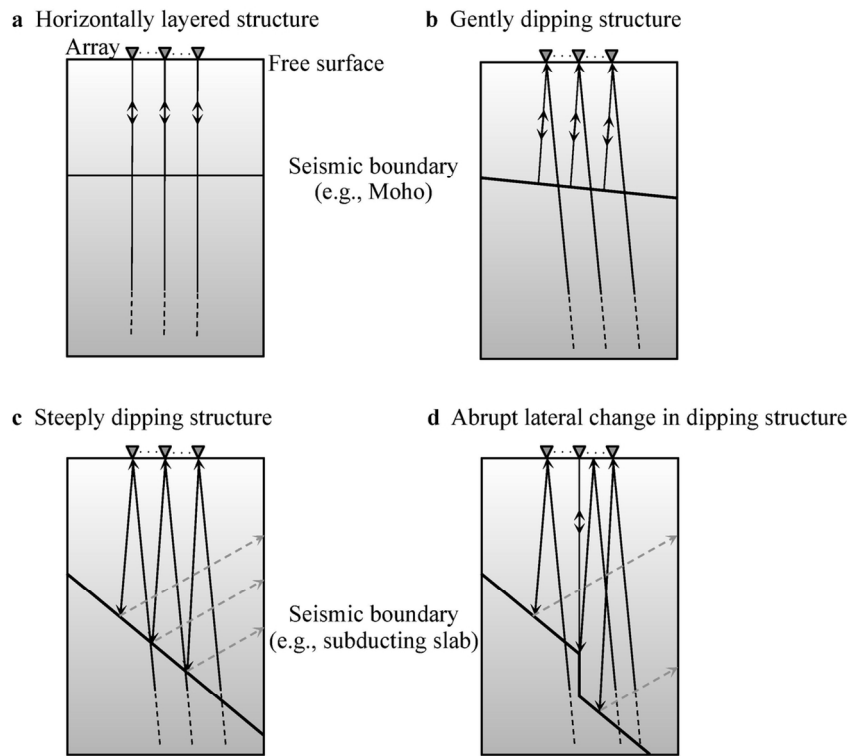


Figure 1. : A schematic illustration of how GloPSI would or would not retrieve reflection responses for: (a) a horizontally layered structure and vertical transmission responses; (b) a gently dipping structure and nearly vertical transmission responses; (c) as in (b), but for a steeply dipping structure; (d) as in (c), but when an abrupt change (e.g., slab deformation) presents in present in the lateral continuation of the dipping structure. The black lines indicate the transmission response from the global earthquakes, while the gray dashed lines depict the reflection response that will not be recorded at the station due to the configuration. Two-way arrows indicate the reflection response that will be recorded at the station.

124x115mm (300 x 300 DPI)

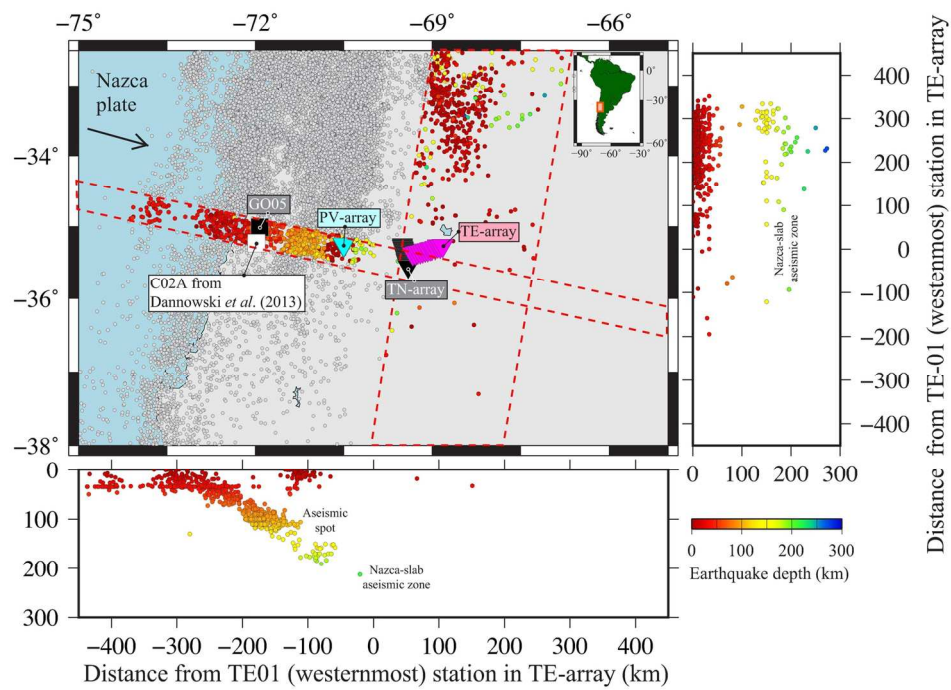


Figure 2. : Center – Location of the seismic stations used in our study, and hypocenters mapping using earthquakes archived by USGS. Below and right – distribution of the hypocenters in depth within the red dashed-line areas in NWW-SEE and NNE-SSW direction.  
153x116mm (300 x 300 DPI)

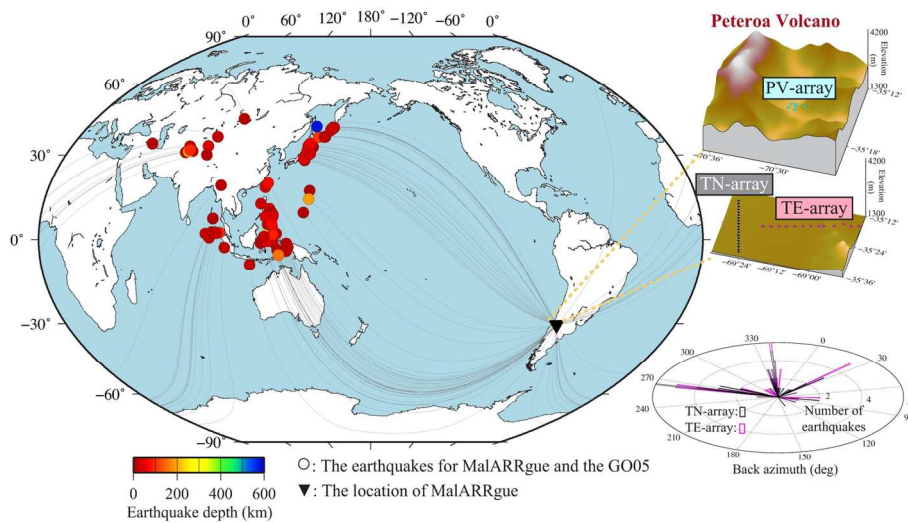
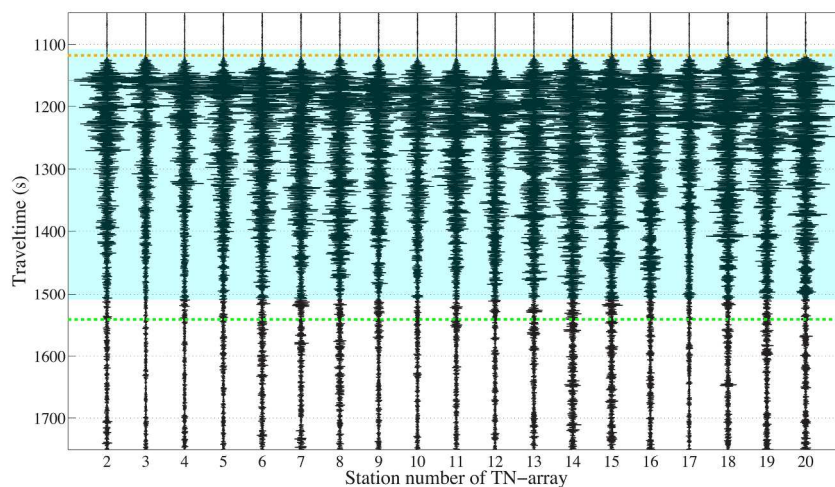
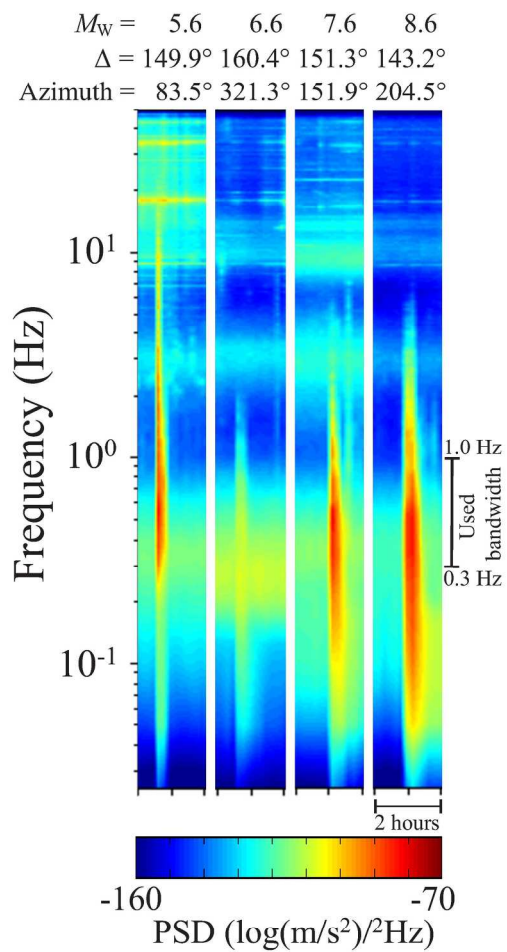


Figure 3. : Distribution of the global-phase earthquakes used in our study. The circles show the location of the earthquakes used for MalARRgue and the GO05 station. The location of MalARRgue is indicated by the black triangle with its topography maps (Becker et al., 2009) in the insets. The distribution of the back azimuth of the earthquakes for the T-array is shown in the inset.  
 149x82mm (300 x 300 DPI)



An example recording of a global earthquake on the vertical component of the stations from the TN-array. The area highlighted in light blue indicates the used window that contains the global phases. The orange and green lines indicate the P- and S-wave phase onsets by IRIS, respectively.  
233x125mm (300 x 300 DPI)



The computed power spectral densities for four earthquakes with different magnitudes that occurred at global distances. The densities are computed for station TE01 of the TE-array in MalARRgue.  $\Delta$  indicates the epicentral distances of the global earthquakes.  
173x246mm (300 x 300 DPI)

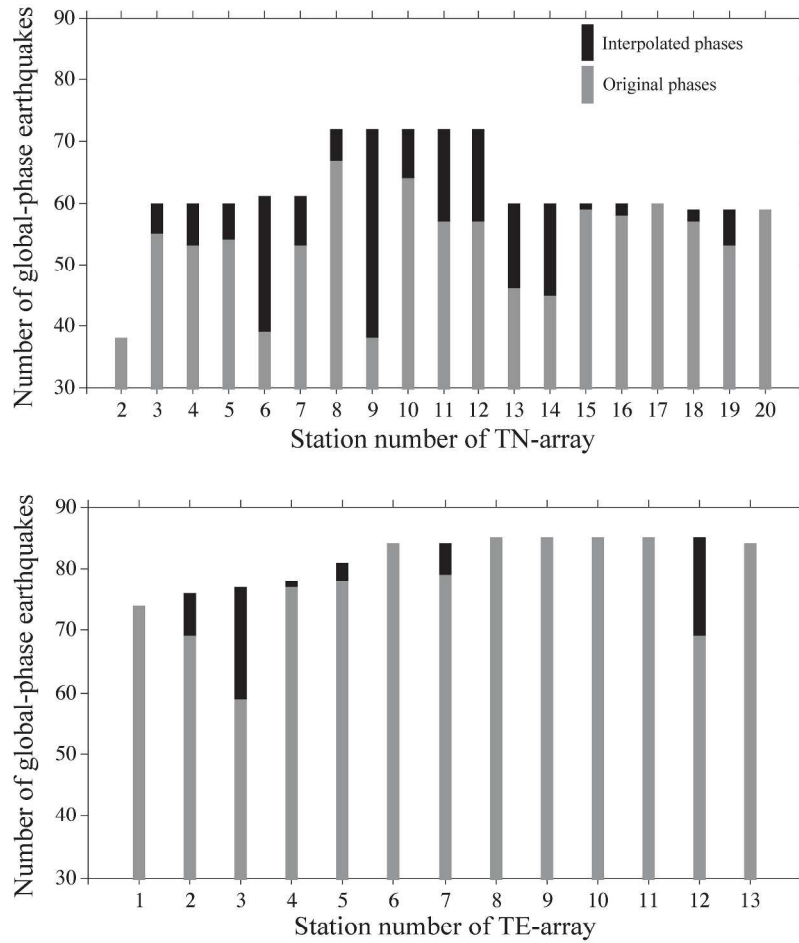


Figure 6. : Number of original and interpolated global phases for TN- (top) and TE-array (bottom) stations. 279x361mm (300 x 300 DPI)

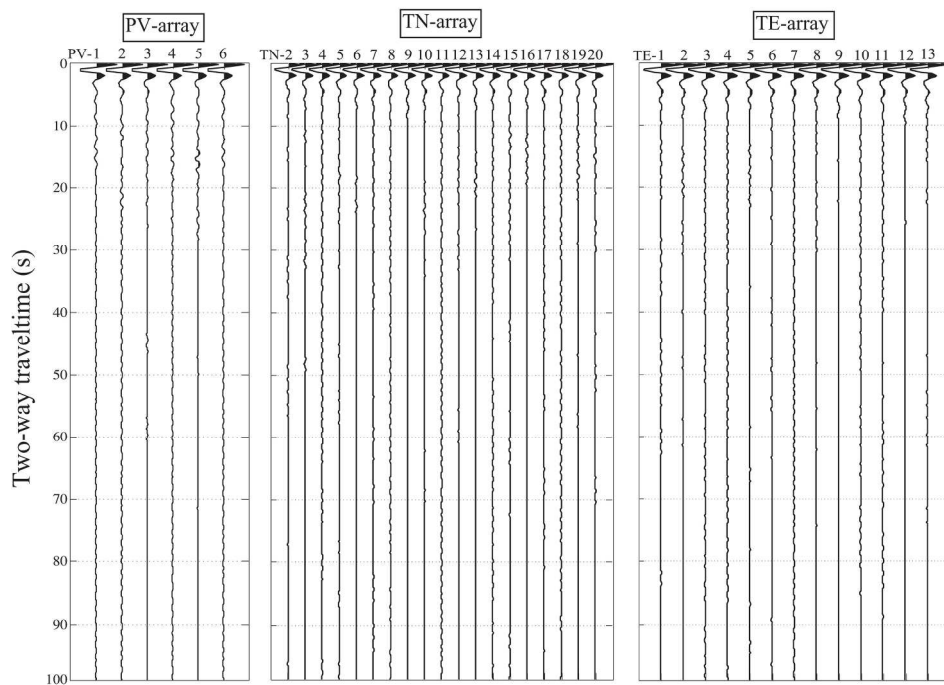


Figure 7. : GloPSI results retrieved at the MalARRgue stations before seismic processing. The annotations along the horizontal axis show the actual station codes.  
 215x166mm (300 x 300 DPI)

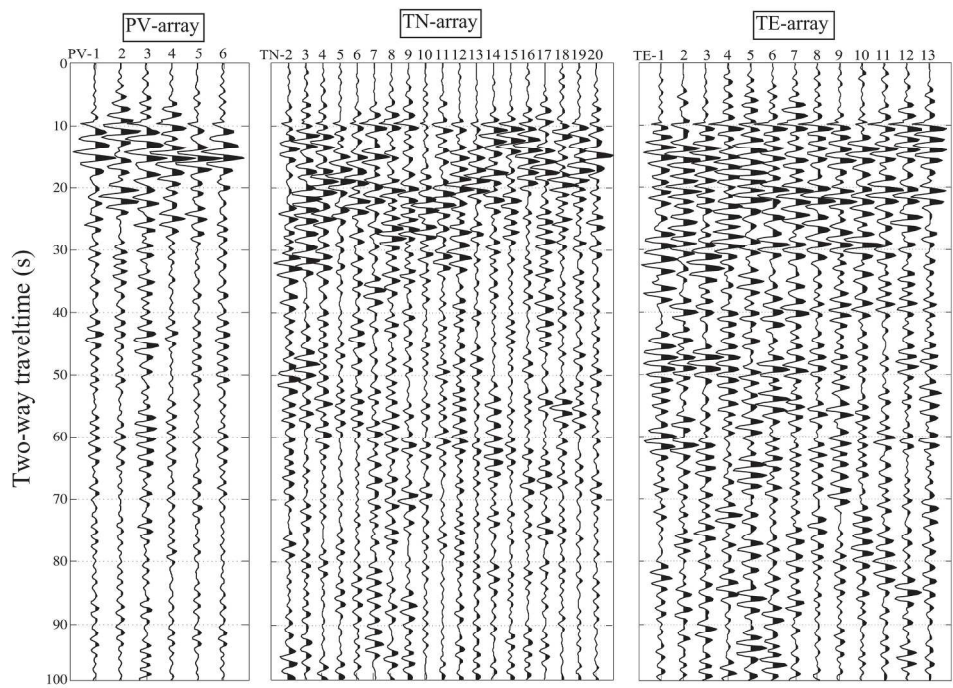


Figure 8. : The results from Figure 7 after subtraction of the mean averaged source time function per subarray.  
215x166mm (300 x 300 DPI)

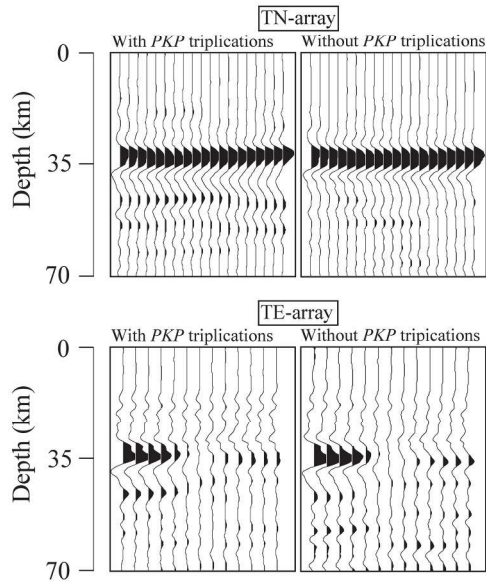


Figure 9. : A comparison of GloPSI images obtained when including and when excluding global phases with PKP triplications. The number of earthquakes for the TN(TE)-array with and without the PKP triplications are 72 (85) and 13 (13), respectively.  
 215x166mm (300 x 300 DPI)

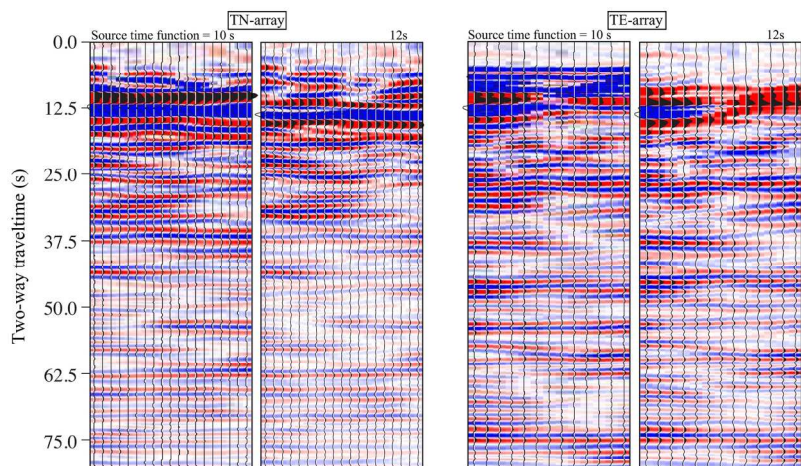


Figure 10. : GloPSI results for the TN- and TE-array after post-stack time migration with lateral smoothing in the offset orientation when respective source time functions of 10 s and of 12 s are used in the estimation of the averaged source time function.  
179x120mm (300 x 300 DPI)

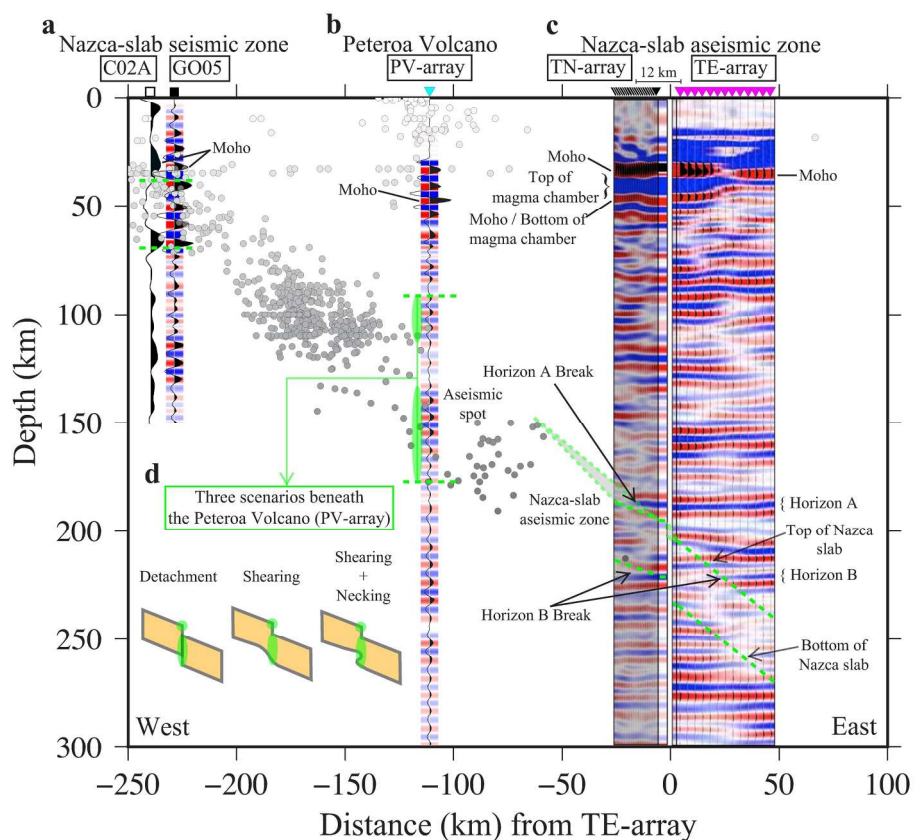


Figure 11. : Summarized interpretation with seismicity along the NWW-SEE area of GloPSI for MalARRgue and station GO05. a. GloPSI for GO05 and receiver function for C02A at the Nazca-slab seismic zone. Moho depth is interpreted using receiver function (Dannowski et al., 2013) at C02A. b. GloPSI for the PV-array beneath the Peteroa Volcano. c. GloPSI for the TN- and TE-array at the Nazca-slab aseismic zone. Dashed green lines in the panels indicate where we interpret the Nazca slab and transparent green rectangles indicate possible interval of the interpretation. The transparent green ellipses indicate where we interpret the Nazca-slab deformation, while the transparent gray triangle – the possible connection between the Nazca-slab seismic and aseismic zones in three dimensions. The insets in the bottom left corner illustrate three possible scenarios explaining the retrieved strong reflectivity below the PV-array. Gray circles (some transparent for visibility purposes) indicate earthquake hypocenters.

206x176mm (300 x 300 DPI)